PREDICTION OF RESIDUAL STRESSES OF REPAIRED AUSTENITIC STAINLESS STEEL WELDED JOINTS

S. HILAL*, S. HENDILI*, J. DELMAS*, P. PEREIRA ALVAREZ*, V. ROBIN**, E. DERNIAUX***, T. BOUTIN*

**Electricité de France R&D, 78400, Chatou, France, sami.hilal@edf.fr*
***Electricité de France Direction Technique, 69007, Lyon, France*
****Electricité de France Direction Technique, 37420, Avoine, France*

10.3217/978-3-99161-089-2-025, license CC BY 4.0

ABSTRACT

The ability to predict residual stresses in welds is important in assessing the integrity of a component subject to degradation mechanisms such as Stress Corrosion Cracking (SCC). In the as-welded condition, multi-pass pipe circumferential butt welds made of austenitic stainless-steel exhibit a typical residual stress profile through the wall of the welded joint. In the case of a non-repaired weld, the shell bending profile places the inner half of the weld joint wall and its vicinity in compression in the axial direction. In contrast, the distribution of residual stresses may be different in the event of a repair, particularly in the case of localised repairs. The impact of repairs on SCC crack propagation was suspected following an inspection of a weld with deep SCC cracks. The particularity of this weld is that it was subjected to two successive repair stages: a complete circumferential repair followed by a localised repair. The specific character of the weld required 3D modelling, since it provides a description of each circumferential zone of the weld and enables verification of the way in which this weld has a particular behaviour (residual stresses, hardness, etc.). This would make it possible to identify potential aggravating factors regarding SCC for this type of weld configuration. This work presents the simulation of this weld, which was carried out in three stages: the initial weld, the first repair, and the localised repair. The expertise carried out following the cutting of the weld made it possible to characterise the strain hardening in the repaired areas and is compared with the simulation results by considering the measurements obtained on a sample taken in the middle of the repair. This comparison is made on hardness profiles in the axial direction of the assembly, at different heights in the thickness. A good correlation is observed between measured and simulated hardness.

Keywords: welding, stress corrosion cracking, pressure water reactor, computational weld mechanics, finite elements, austenitic stainless-steel.

INTRODUCTION

At the end of 2021, EDF (Electricité de France) began detecting indications on the Safety Injection System (SIS) piping in the French nuclear fleet. Expert assessments revealed the presence of cracks associated with primary water Stress Corrosion Cracking (SCC) phenomenon, located at welds on stainless steel components [1] [2]. Many numerical welding simulations were carried out by EDF to better understand the origin of the phenomenon and the role of welding. Furthermore, these welding simulations were exploited as input data for SCC simulations to assess crack initiation conditions and propagation rates under this damage mechanism [1]. The numerical welding simulation approach is based on finite element modelling of the thermomechanical behaviour of a structure during welding. The methodology follows the French Nuclear Institute (CEA/EDF/FRAMATOME) Good Practice Guide for Numerical Welding Simulation, which is based on the ISO/TS 18166 standard: Numerical Welding Simulation [3]. A 2D axisymmetric modelling assumption is adopted for multi-pass butt welds [1]. The quantities computed in these simulations include welding residual stresses (WRS), local deformations, hardness (via post-processing of calculated strain hardening [4]), the as-welded residual state, and the redistribution of these stresses under service loading. The results are presented as maps showing the influence of the manufacturing process on the local residual state, and through parametric studies to understand the influence of selected parameters (e.g., process parameters, geometry) on stress and deformation trends [1]. In agreement with the literature [5] and operational feedback, simulations of unrepaired welds performed to date show that, in the as-welded state, multi-pass circumferential butt welds on austenitic stainless-steel piping exhibit a typical “S-shaped” residual stress profile across the weld thickness (Fig. 1).

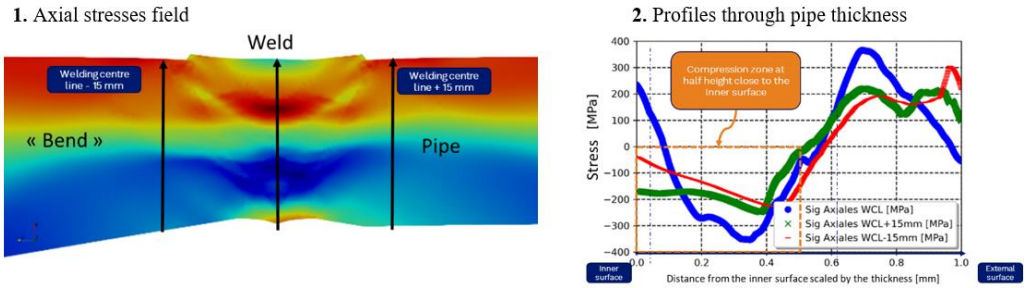

Fig. 1 Typical axial stress state from simulation performed on a 12’’ schedule 140 (28.58 mm thick) pipe assembly [1]: 1. 2D axial stress field, 2. Profiles through thickness

The welds studied using numerical welding mechanics show a compressive axial stress state over half the thickness from the inner surface, which tends to slow down or even stop potential crack propagation. Near the weld root, the stress state may evolve toward tension at the end of the operation. Differences in stiffness across the weld (e.g., a weld on a pipe elbow), as well as the welding completion sequence, can influence the distribution of tensile stresses

in the root area. Residual stresses result from the development of permanent deformations in the weld zone subjected to successive thermal cycles during welding, as illustrated by numerical modelling [6]. Strain hardening accumulates, altering the local mechanical behaviour and creating a TMAZ in the austenitic stainless steel. This numerical welding simulation approach has been applied to many studies supporting the primary water SCC issue on austenitic stainless-steel SIS. It has also been used to conduct parametric studies to identify the most influential parameters and to ensure the systematic presence of the compressive zone [1].

In 2023, the most severe case of intergranular SCC was reported at the French nuclear power plant located in Penly, specifically within the hot leg of the Safety Injection System. A stress corrosion crack measuring 23 mm in depth was detected in the heat-affected zone (HAZ) of a weld that had undergone a full-depth repair extending over 50° of the pipe's circumference during fabrication. Notably, the crack propagation was confined to the repaired section and did not initiate in the non-repaired areas of the weld. A cross-section analysis centred on the double-repair zone revealed a 23 mm deep crack within the HAZ, along the base metal/filler metal interface. The weld's manufacturing history involved two successive repair operations: an initial *cut-and-weld*, followed by a localised repair on a limited segment of the pipe circumference. Expert assessments enabled the evaluation of hardening levels through hardness mapping performed on multiple samples. The results did not indicate any significant hardening around the repair zone that could explain either the localised initiation of SCC or the extensive crack propagation observed in this weld. Nevertheless, this recent operational experience underscores the potentially adverse impact of weld repairs on SCC susceptibility. Furthermore, according to EDF's SCC propagation model for stainless steels exposed to primary water, crack growth rates are influenced by the combined effects of residual stresses and plastic strain. Therefore, the distribution and magnitude of residual stresses are key factors contributing to SCC propagation.

The objective of the present study is to evaluate the residual condition of the welded assembly, thereby complementing the findings of the expert assessments and identifying aggravating factors associated with SCC in this specific welding configuration. To achieve this, and considering the weld's unique characteristics, an advanced approach mixing two-dimensional axisymmetric and three-dimensional numerical welding simulations is performed to predict the residual stress field and plastic strain distribution throughout the entire welded structure.

DESCRIPTION OF THE INVESTIGATED WELD JOINT

The assembly studied is a 316L stainless steel "elbow-to-elbow" configuration with a diameter of 10 inches and a thickness of 25.4 mm. The specificity of this assembly is that the weld was subjected to two successive repair operations. Fig. 2 schematically illustrates the various step-by-step stages of assembly.

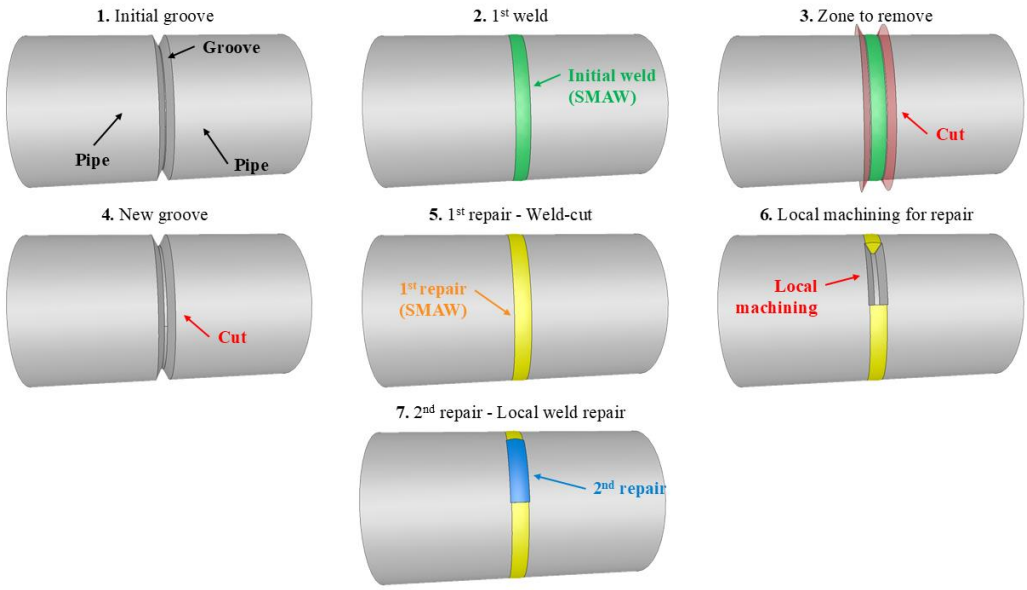

Fig. 2 Schematic illustration of the different stages of the repaired assembly

The first stage of the process involves the initial weld, referred to as the *workshop weld* (Fig. 2.1 and Fig. 2.2). This weld was performed using the Shielded Metal Arc Welding (SMAW) process, with a "W-joint" groove configuration featuring angles of 45° and 30° on each side. For this manufacturing step, a Welding Procedure Specification (WPS) was available, along with a macrograph of a different weld produced using the same process.

Following the completion of the initial weld, a full circumferential repair known as a *cut-and-weld* was carried out. This operation was performed in two stages. First, the existing weld was removed, to eliminate part of the fusion zone (Fig. 2.3 and Fig. 2.4). Once the excavation was completed, the repair weld was carried out on the full circumference using the SMAW process (Fig. 2.5).

Subsequently, a localised excavation was performed on the internal surface over an angular span of 50°, extending through the full thickness of the joint (Fig. 2.6 and Fig. 2.7), to perform another repair, a localised one. This second repair was also executed using the SMAW process.

It is important to note that the weld was evaluated through macrographic analysis at various circumferential sections. As a result, macrographs are available both within the second repair zone and outside of it. The macrograph corresponding to the area unaffected by the second repair is considered representative of the cut-and-weld configuration (Fig. 3.1).

Based on the interpretation of the WPS and the macrographs analysis, the geometries of the repairs and weld beads were defined. For the *cut-and-weld* configuration, the groove angle identified was approximately 25° (V-joint groove). For the second repair, the macrographic analysis (Fig. 3.2) revealed also a groove angle of 25° (V-joint groove), with a width of 7.5 mm on the inner surface and an external width of 30 mm.

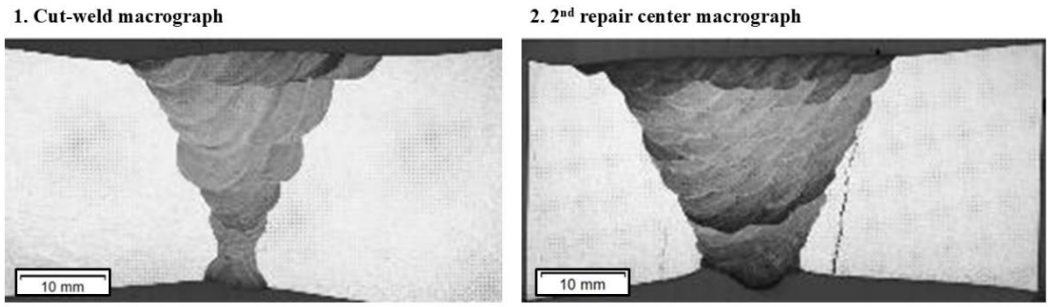

Fig. 3 Macrograph acquired after characterization of the weld: in the area of the *cut-and-weld* and in the area with local repair

Finally, hardness mappings ($HV_{0.5}$) were performed at various circumferential weld cross-sections, particularly at the centre of the localized repair and on the opposite side (Fig. 4). These measurements will be compared with simulation results to validate the modelling approach.

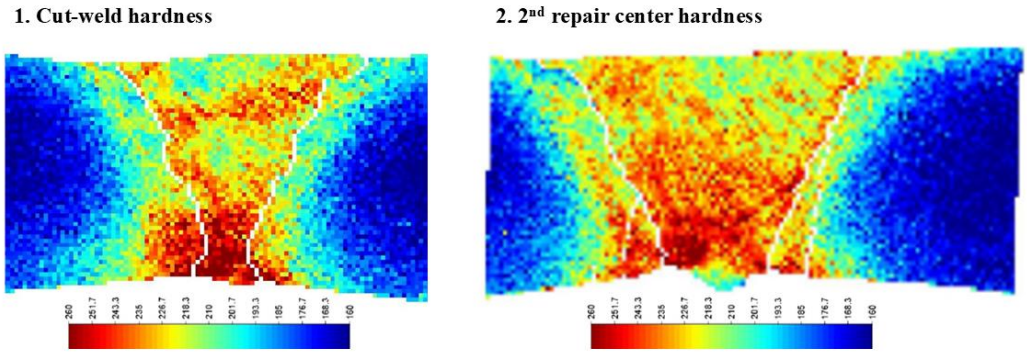

Fig. 4 Hardness mappings: (1) after the first repair cut-and-weld, (2) after the second local repair

GENERAL METHODOLOGY AND SIMULATION WORKFLOW

The models considered in this study have been developed using Pipeweld [7], a simulation framework dedicated to computational welding simulation based on code-aster [8], an open-source generalist finite element software of simulation in mechanics and in structural analysis developed by EDF for more than 30 years, integrated within the salome-meca platform [9].

Without externally applied loads, the mechanical impact of welding is primarily driven by thermal gradients within the thermo-mechanically affected zone (TMAZ). Defining the thermal loading is crucial for identifying the stress fields that lead to WRS. These stresses arise from local elastic and inelastic responses, compounded by global internal forces due to

self-bridging effects from colder, more rigid regions. In multi-pass welding, repeated cycles of thermal expansion and contraction are constrained by these stiffer zones, contributing to the development of WRS. As illustrated in Fig. 5, a weak coupling approach, based on the sequential execution of thermal, metallurgical, and mechanical analyses at each welding pass, is sufficient to predict the WRS for the assemblies under consideration.

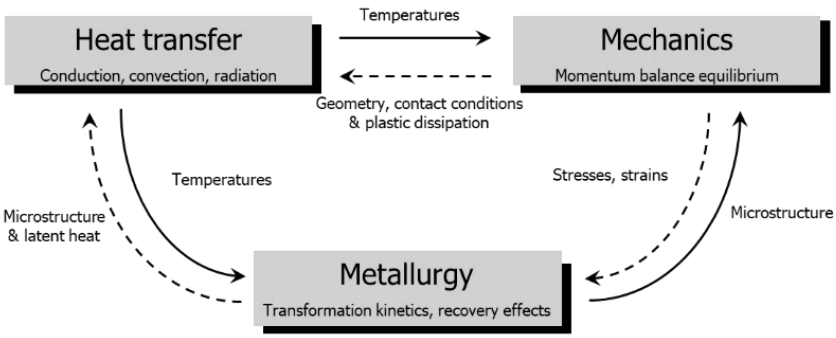

Fig. 5 Coupling and interaction for WRS assessment: heat transfers, metallurgical phenomena and mechanical consequences

First, the thermal analysis is performed, and its results are subsequently used as input data for the mechanical analysis. The thermal problem is governed by the classical heat conduction equation, where the heat input is modelled as a volumetric density heat flux, with a triangular distribution and uniform along the transverse direction of the weld path. The heat source distribution is mathematically described by the following expressions (with Ω the volume):

$$E = \eta UI = \int_{\Omega} Q(x,y,z).d\Omega = Q_{max} \times S_b \times (\Delta t_1 + \Delta t_2) \times 0.5 \quad (1)$$

$$Q_{max} = \frac{2 \times \eta \times Q}{V_s \times S_b \times (\Delta t_1 + \Delta t_2)} \quad (2)$$

where E, Q, η, V_s, S_b, and Δt_1 and Δt_2 represent the net welding energy, the power, the efficiency, the welding speed, the bead cross-section surface and the heat source morphological parameters. Thermal boundary conditions, that include both convective and radiative heat exchanges with the surrounding ambient air.

The evolution of WRS depends on the constitutive laws linking stress and strain, which typically include elastic, thermal, and inelastic parts. Of particular importance is the modelling of plasticity, responsible for permanent deformation and the development of WRS. The mechanical response, driven by the thermal field, is assumed to follow an elasto-plastic behaviour with isotropic hardening. The elastic properties are characterized by Young's modulus, Poisson's ratio, and the coefficient of thermal expansion. Plastic deformation is described using the Von Mises yield criterion combined with a non-linear isotropic hardening law. The hardening behaviour, which depends on both plastic strain and temperature, is derived from stress-strain curves obtained through experimental measurements. The constitutive model employed here incorporates work hardening recovery mechanisms, defined

to describe the behaviour of alloys that do not undergo solid-state phase transformations during welding, such as austenitic stainless steels. The equations for the constitutive behaviour of the material are detailed in the following paragraph.
First, the Von Mises equivalent stress is expressed as follows:

$$f(\sigma_{ij}) = \sigma_{eq} = J_2(s_{ij}). \tag{3}$$

The yield strength of the strain-hardened material is written:

$$\sigma_y(p,\theta) = \sigma_0(\theta) + R(p,\theta), \qquad p = \int_0^t {\dot{\varepsilon}_{eq}}^p . dt \ , \qquad {\dot{\varepsilon}_{eq}}^p = \dot{p} = \sqrt{\frac{2}{3}\dot{\varepsilon}_{ij}^p . \dot{\varepsilon}_{ij}^p} \tag{4}$$

with p the cumulative plastic strain, R the hardening function, σ_0 the initial yield strength and θ the temperature.

The recovery of work hardening is modelled by the following equation [10]:

$$\dot{r}(t) = \dot{p}(t) - k(\theta(t))\langle r(t) - r_\infty(\theta(t))\rangle \tag{5}$$

with r the cumulated plastic strain with consideration of the strain hardening recovery, k the coefficient which characterizes the dynamics of recovery according to the temperature and which depends on the considered material, r_∞ the coefficient which characterizes the threshold quantity of plastic deformation which cannot be recovered, and which depends on the temperature and the considered material, and $\langle x \rangle$ which denotes the positive part of x.

In the context of SCC, in addition to residual stresses, strain hardening also plays a significant role (initiation and propagation mechanisms) [2]. The strain hardening, often represented by the equivalent plastic strain, is typically computed implicitly during numerical welding simulations and has been shown to correlate directly with hardness measurements. The same relationship that the one established in [4] between strain hardening and hardness is used:

$$HV = HV_{min} + A(1 - e^{-Bp}) \tag{6}$$

The coefficients HV_{min}, A, B are correlated with microhardness measurements performed on the base metal of welds cut and deposited in the French nuclear fleet.

Table 1 Correlated coefficient for the relationship between strain hardening and hardness

HV_{min}	A	B
160	176,93	0,046

The proposed approach consists of using 2D for the *initial weld* step and the *cut-and-weld* step because the axisymmetric assumption is considered sufficient for fully circumferential welding operations. Nevertheless, it is essential to consider a fully three-dimensional approach for the third step. A detailed description of each modelling step is provided below. It is important to note that for 2D axisymmetric simulations, the mesh is composed of quadrilateral elements, whereas hexahedral elements are used for the 3D simulations. Thermal simulations, both in 2D and 3D, are performed using linear elements. In contrast, mechanical simulations in 2D and 3D are conducted with quadratic elements and use a reduced integration formulation.

STEP 1: 2D INITIAL WELD SIMULATION

The first weld is modelled using a 2D axisymmetric finite element approach. The mesh is constructed based on the groove geometry and the number of welding beads, as defined in the welding procedure specification. Process parameters such as heat input and welding speed are also derived from this specification. Due to the 2D axisymmetric assumption, mechanical boundary conditions representing self-restraint are applied to simulate the stiffness of the "cold" regions of the pipe during the heating phase.

STEP 2: 2D MODELLING OF THE CUT-AND-WELD REPAIR

Fig. 6 illustrates the modelling methodology for the repair weld, commonly referred to as the cut-and-weld process. Given its fully circumferential nature, this stage is also modelled using a 2D axisymmetric approach. The process consists of two main steps. The first involves material removal, for which the deformed mesh from the initial weld simulation is used as the base geometry. The groove geometry after excavation, as well as the subsequent filling, is defined based on macrographic analysis conducted during failure investigations. A mechanical rebalancing is performed to determine the initial stress state of the pipe prior to the deposition of the new weld. The second step involves filling the groove. The number and sequence of welding passes are inferred from macrographic observations. Process parameters are selected using an internal synergy approach, which reconciles macrographic data with the welding procedure qualification record. As in the initial weld simulation, self-restraint boundary conditions are applied due to the axisymmetric modelling assumption.

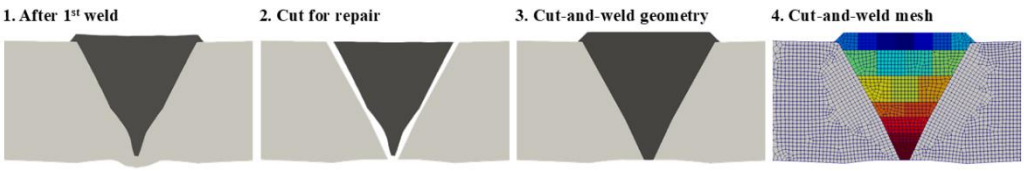

Fig. 6 Illustration of the required steps for generating the mesh for the cut-and-weld simulation

STEP 3: 3D MODELLING OF THE LOCALISED SECOND REPAIR

Due to the localised and non-axisymmetric nature of the second repair, this stage is modelled in 3D. To define a compatible initial stress state, the axisymmetric residual stress field from the previous cut-and-weld simulation is mapped onto a three-dimensional structure. This is followed by the modelling of the excavation, which defines the geometry of the assembly after material removal in the repair zone. The excavation profile is modelled with steeper slopes at the ends, and the cross-section and maximum depth are assumed constant along the repair length. The residual stress state after excavation is obtained through a mechanical rebalancing calculation. The sequence of steps used to compute the residual stress field following

excavation of the cut-and-weld repair is illustrated in Fig. 7. Regarding mechanical boundary conditions, three points located at the pipe extremities are constrained to prevent rigid body motion while allowing realistic deformation behaviour.

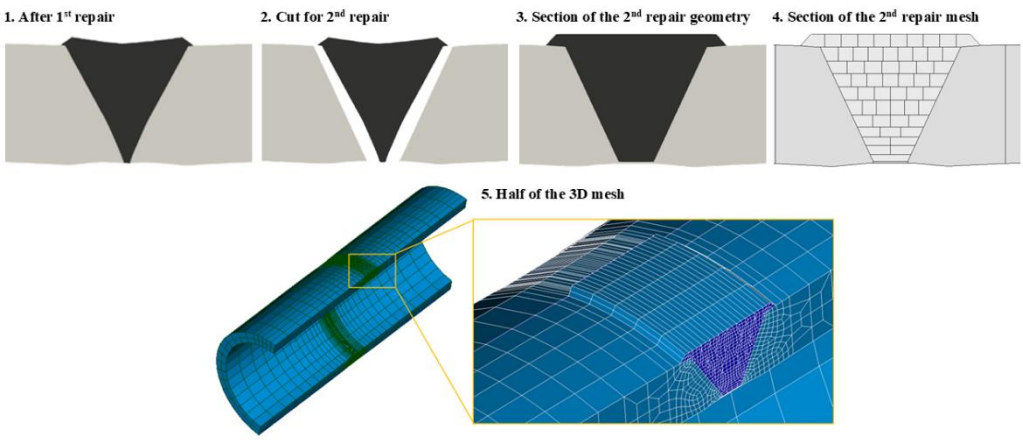

Fig. 7 Illustration of the required steps for generating the mesh for the local repair simulation

The study was conducted in three main phases (Fig. 8). Initially, a simulation of the welding process was performed. Subsequently, the deformed geometry was extracted to generate a new mesh for the post-weld cut simulation. A two-dimensional simulation of the post-weld cut was then carried out.

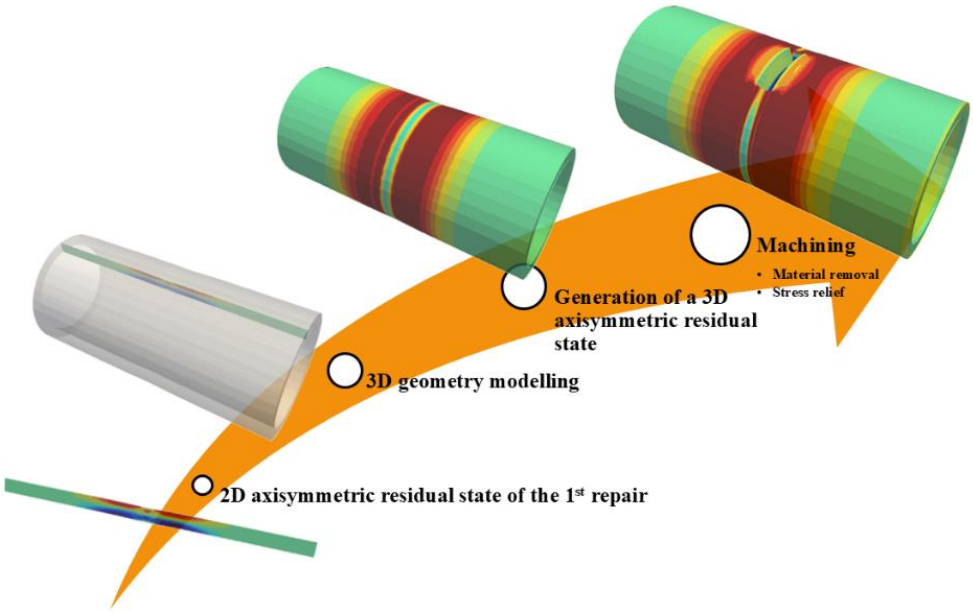

Fig. 8 Advanced modelling approach: modelling steps of local weld excavation

RESULTS AND DISCUSSIONS

The computational time for the 2D simulations ranged from approximately 3 to 5 hours, whereas the three-dimensional simulation required around 50 hours on a HPC cluster with 36 CPU.

The results of the study are presented in two stages. First, the initial weld, the post-weld cut, and its mechanical effects are described. This is followed by the presentation and discussion of the results from the second repair phase, which involved a localised repair strategy.

ANALYSIS OF THE INITIAL WELD AND POST CUT-AND-WELD

Fig. 9 illustrates the axial stress and hardness distributions obtained at each stage of the welding process, up to and including the post-weld cut: the initial weld, the rebalancing phase following excavation, and the first repair weld. At the end of the repair process, the axial stress distribution around the weld joint is characterised by a tensile zone near the inner surface, followed by a compressive region extending to mid-thickness, and then a return to tensile stress near the outer surface.

As shown in Fig. 9, strain hardening increases significantly in the HAZ along the groove edges. Notably, the strain-hardened region in the root bead area is both deeper and more extensive through the thickness compared to that observed during the initial fabrication.

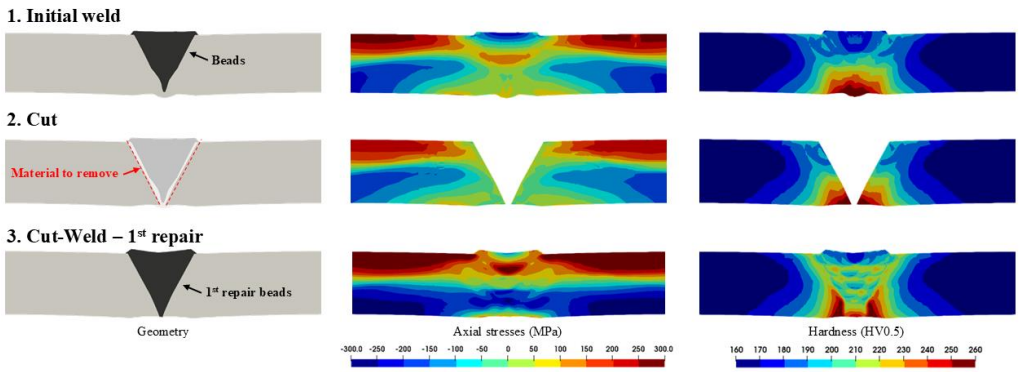

Fig. 9 Axial residual stress (MPa) and microhardness ($HV_{0.5}$) distributions at three stages: initial weld (prior to excavation), following excavation, and after cut-and-weld

A metallurgical assessment conducted after weld removal enabled the characterisation of strain hardening on samples extracted from the side opposite the repaired zone (Fig. 10). The hardness measurements obtained from these samples are considered unaffected by the repair process. Therefore, they are deemed representative of the residual state prior to repair, corresponding to the post-cut condition of the initial weld.

These experimental results were compared with simulation outputs by evaluating axial hardness profiles at various depths through the thickness (Fig. 11). The origin of the horizontal axis corresponds to the interface between the fusion zone and the base material. A strong correlation was observed between the measured and simulated hardness values, particularly in the vicinity of the fusion zone, with both exhibiting similar magnitudes and trends along the axial direction.

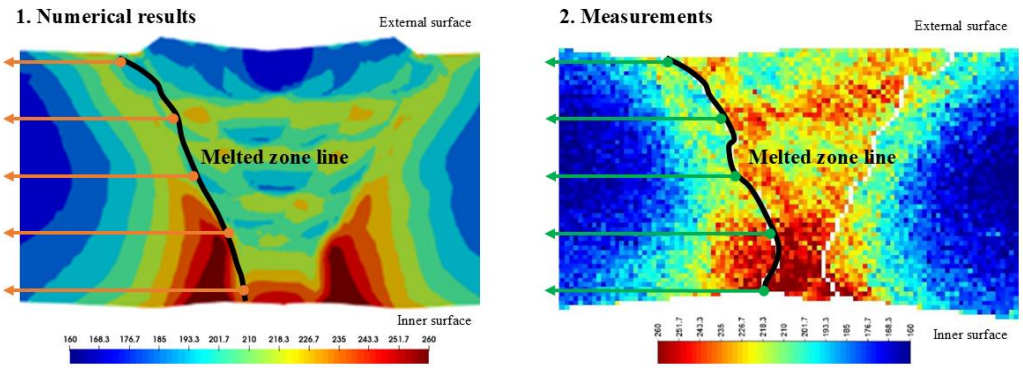

Fig. 10 Hardness after cut-and-weld: 1. Numerical results, 2. Measurements

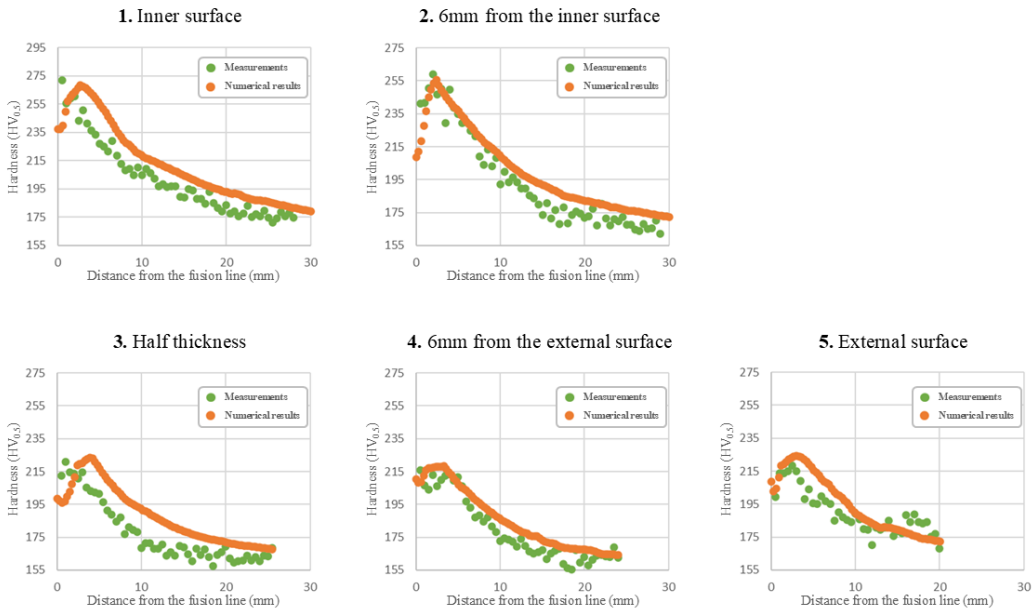

Fig. 11 Comparison of experimental and numerical results after the cut-and-weld: hardness profiles measured along the longitudinal axis of the assembly at different depths through the pipe thickness

ANALYSIS OF THE LOCALISED REPAIR

Fig. 12 presents an analysis of axial residual stresses and hardness distributions obtained from a 2D cross-section taken along a median plane of the structure, perpendicular to the axis of

revolution of the assembly. This analysis highlights the localised impact of the repair on the residual state of the assembly, which is confined to a narrow region surrounding the repaired area. Specifically, the residual stress field exhibits a significant reduction in compressive stress through the thickness, while the hardness levels are generally higher in the repaired zone, with a broader and deeper affected region within the pipe thickness. It is also noteworthy that the repair process perturbs the residual state only within a limited area adjacent to the repair. The remainder of the pipe structure remains largely unaffected.

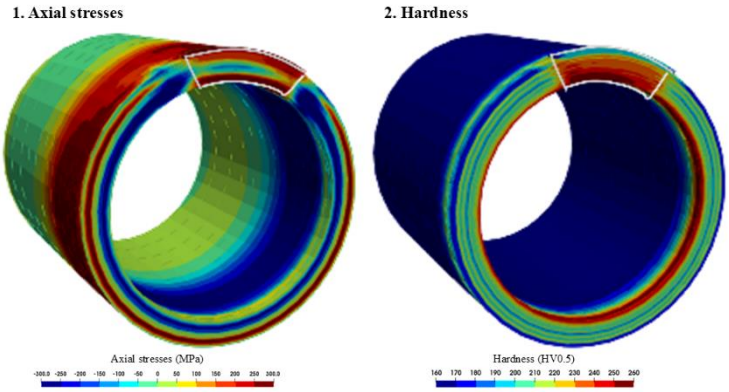

Fig. 12 Three-dimensional distribution of axial residual stresses (MPa) and hardness ($HV_{0.5}$) represented on a cross-sectional view taken along the mid-plane of the welded joint

To further investigate this behaviour, cross-sections at various azimuthal positions were extracted (Fig. 13). These 2D sections (Fig. 14) reveal atypical residual stress distributions when compared to those observed in unrepaired welds. In particular, relative to prior simulation data for non-repaired welds, the axial stress field in the inner surface exhibits a more pronounced tensile character, with greater depth and extent from the inner wall. Additionally, the compressive zone is weaker and less extensive, and in some cases, nearly absent, especially at the initiation point of the repair.

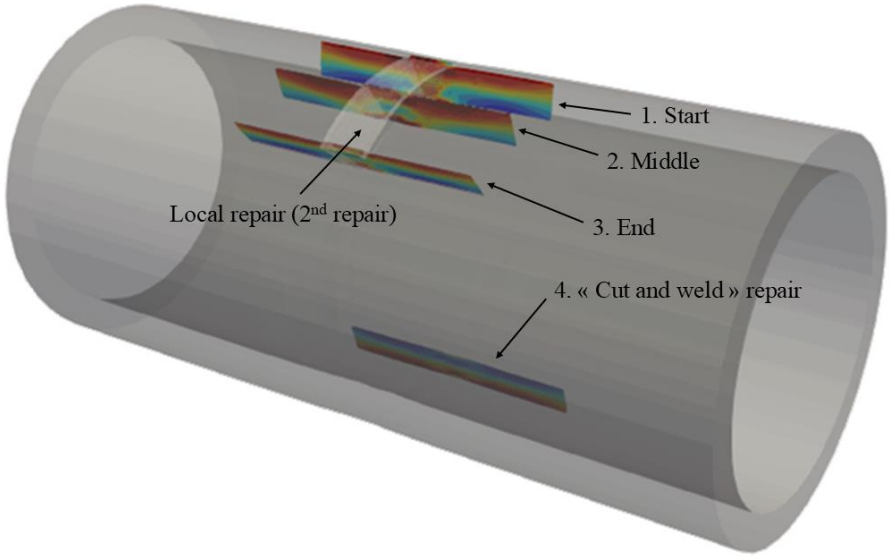

Fig. 13 Axial stress extraction at selected locations: within the repair zone (positions 1: start, 2: middle, 3: end) and outside the repair (position 4: opposite side of the local repair)

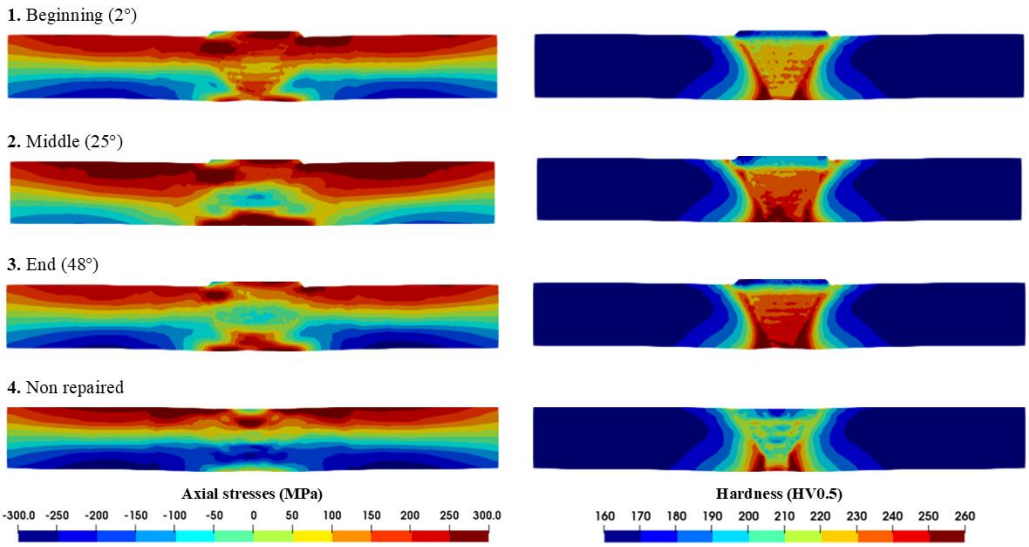

Fig. 14 Distributions of axial residual stresses (MPa) and hardness ($HV_{0.5}$) extracted at different circumferential locations of the pipe, including the repaired region (start, middle, and end) and a reference position outside the local repair zone

A metallurgical assessment enabled the characterisation of the hardness within the local repair zone (Fig. 15). The results of this assessment were compared with simulation outputs using hardness measurements obtained from a sample extracted at the mid-length of the repair (Fig. 16). This comparison was performed by evaluating axial hardness profiles at various depths through the thickness of the assembly. A strong correlation was observed between the measured and simulated hardness values.

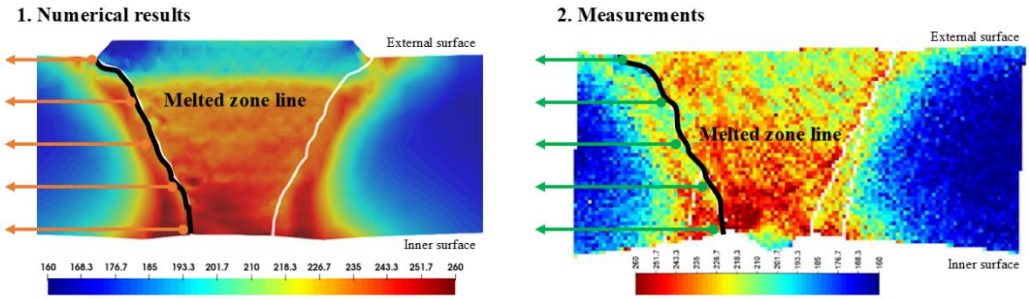

Fig. 15 Hardness after local repair (middle section): 1. Numerical results, 2. Measurements

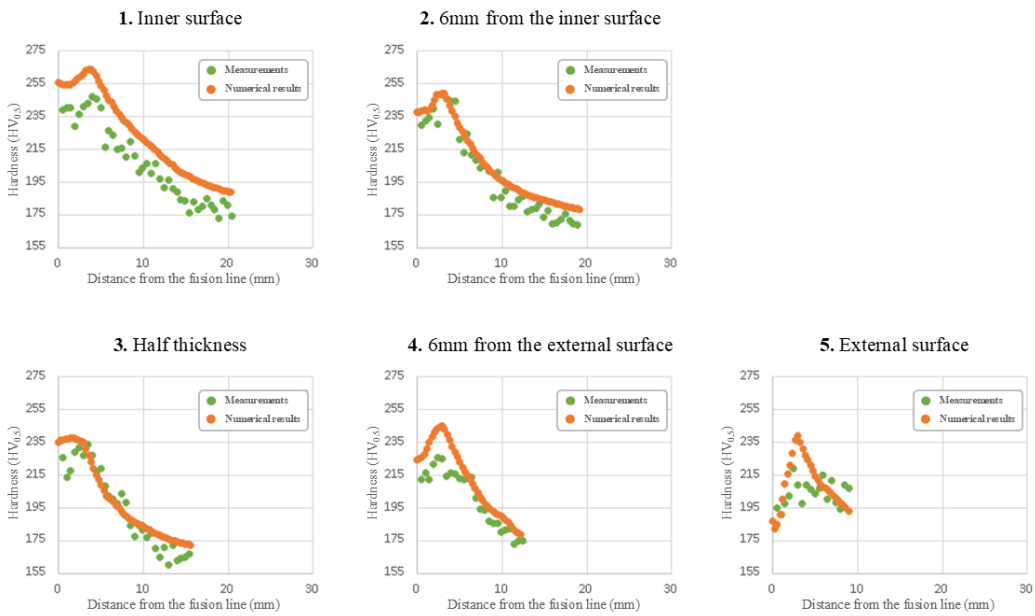

Fig. 16 Comparison of experimental and numerical results after the local repair: hardness profiles measured along the longitudinal axis of the assembly at different depths through the pipe thickness

DISCUSSION

The numerical methodology employed in this study, integrating sequential simulations of the initial weld, post-weld cutting, and localised repair, has demonstrated its effectiveness in accurately capturing the mechanical behavior of the assembly. The strong correlation between simulated and experimental data, particularly in hardness profiles, underscores the reliability of the modeling approach.

Firstly, the cut-and-weld operations (fully repaired welds) do not appear to increase the risk of SCC compared to unrepaired welds, based on axial stress levels and hardness measurements. Moreover, a key finding of this study is the highly localized nature of the repair's impact. The residual stress field and strain hardening are significantly modified in the immediate vicinity of the repaired zone, while the rest of the pipe structure remains largely unaffected. This observation is particularly important, as it suggests that localised repairs do not compromise the overall mechanical integrity of the assembly.

Furthermore, the residual stress distributions in the locally repaired zones exhibit atypical characteristics compared to those in unrepaired welds. Notably, tensile stresses near the inner surface are more pronounced and penetrate deeper into the material thickness, while the compressive zone is diminished or even absent in certain regions. These deviations from the typical “S-shaped” stress profiles observed in unrepaired welds may account for the increased susceptibility to SCC.

The comparison between simulated and measured hardness profiles further supports the model’s predictive capability. The consistency observed across different depths and axial positions reinforces the validity of the simulation framework.

CONCLUSION

This study highlights the effectiveness of a multi-step numerical approach in simulating the mechanical effects of a twice-repaired weld: a fully circumferential cut-and-weld repair followed by a localised weld repair. The main conclusions are as follows:

- The fully repaired weld does not exhibit an increased risk of SCC compared to unrepaired welds, based on axial stress and hardness evaluations.
- The localised repair induces targeted modifications in the residual stress and hardness fields, with minimal influence on the rest of the structure.
- In the localised repair, tensile stresses near the inner surface are more pronounced and extend deeper into the thickness, while the compressive zone is reduced or even absent in certain areas. These deviations may account for the increased susceptibility to SCC.
- The simulation results show strong agreement with experimental measurements, confirming the accuracy and robustness of the numerical model.

Future work will aim to extend the study to various localised repair geometries, with the objective of identifying the most influential repair geometrical features in relation to primary water SCC susceptibility.

References

[1] V. ROBIN, S. HENDILI, J. DELMAS, S. HILAL, D. IAMPIETRO, M. ABBAS and S. JUTTEAU: 'Modelling of residual stresses in multi-pass pipe circumferential butt welds made of austenitic stainless steel to provide indicators for SCC risk classification', *Proceedings of the ASME 2023 Pressure Vessels and Piping Conference,* PVP2023-107448, 2023.

[2] T. COUVANT, C. VARÉ, J. M. FRUND, S. LECLERCQ, Y. THÉBAULT, N. ETCHEGARAY, J. DELMAS: 'Susceptibility to SCC of cold work austenitic stainless steels in non-polluted primary PWR environment', *Proceedings of FONTEVRAUD 10 conference*, September 19 to 22, Avignon, France, 2022.

[3] CEN ISO/TS 18166:2016, *Numerical welding simulation - Execution and documentation*, 2015.

[4] O. MURÁNSKY ET AL.: 'The influence of constitutive material models on accumulated plastic strain in finite element weld analyses', *International Journal of Solids and Structures,* Vol. 69, pp.518-530, 2015.

[5] P. DONG ET AL.: 'On residual stress prescriptions for fitness for service assessment of pipe girth welds', *International Journal of Pressure Vessels and Piping,* 123-124, pp. 19-29, 2014.

[6] P. DURANTON, J. DEVAUX, V. ROBIN, P. GILLES, J.-M., BERGHEAU: '3D modelling of multipass welding of a 316L stainless steel pipe', *J. Mat. Proc. Tech.*, 153-154, pp. 457-463, 2004.

[7] J. DELMAS, S. HENDILI, P. PEREIRA ALVAREZ, S. HILAL and V. ROBIN: 'Pipeweld, a software suite for computational welding mechanics for nuclear applications', *Proceedings of the 14th International Seminar "Numerical Analysis of Weldability",* 21 - 24 September, Graz - Castle Seggau, Austria, 2025.

[8] ELECTRICITÉ DE FRANCE: 'Finite element code-aster: Analysis of Structures and Thermomechanics for Studies and Research', Open source on www.code-aster.org, 1989-2025.

[9] J. DELMAS, A. ASSIRE: 'Salome-Meca : une plate-forme au service de la simulation mécanique', *Proceedings of the 9ème Colloque National en Calcul des Structures CSMA 2009,* 2009. url: https://hal.archives-ouvertes.fr/hal-1413149.

[10] S. HENDILI, L. LE GRATIET, M. ABBAS: 'Un nouveau modèle simplifié de la restauration d'écrouissage utilisé dans la simulation numérique du soudage', *Proceedings of the 13ème Colloque National en Calcul des Structures CSMA 2017,* 2017.